The Astrophysical Journal, 734:84 (13pp), 2011 June 20 doi:10.1088/0004-637X/734/2/84

SOLAR SOURCE AND HELIOSPHERIC CONSEQUENCES OF THE 2010 APRIL 3 CORONAL MASS EJECTION: A COMPREHENSIVE VIEW

Ying Liu[1], Janet G. Luhmann[1], Stuart D. Bale[1], and Robert P. Lin[1,2]
[1] Space Sciences Laboratory, University of California, Berkeley, CA 94720, USA; liuxying@ssl.berkeley.edu.
[2] School of Space Research, Kyung Hee University, Yongin, Gyeonggi 446-701, Republic of Korea
Received 2011 February 28; accepted 2011 April 7; published 2011 May 27

ABSTRACT

We study the solar source and heliospheric consequences of the 2010 April 3 coronal mass ejection (CME) in the frame of the Sun–Earth connection using observations from a fleet of spacecraft. The CME is accompanied by a B7.4 long-duration flare, dramatic coronal dimming, and EUV waves. It causes significant heliospheric consequences and space weather effects such as radio bursts, a prominent shock wave, the largest/fastest interplanetary CME at 1 AU since the 2006 December 13 CME, the first gradual solar energetic particle (SEP) events in solar cycle 24, and a prolonged geomagnetic storm resulting in a breakdown of the *Galaxy 15* satellite. This event, together with several following periods of intense solar activities, indicates awakening of the Sun from a long minimum. The CME EUV loop begins to rise at least 10 minutes before the flare impulsive phase. The associated coronal wave forms an envelope around the CME, a large-scale three-dimensional structure that can only be explained by a pressure wave. The CME and its preceding shock are imaged by both *STEREO A* and *B* almost throughout the whole Sun–Earth space. CME kinematics in the ecliptic plane are obtained as a function of distance out to 0.75 AU by a geometric triangulation technique. The CME has a propagation direction near the Sun–Earth line and a speed that first increases to 1000–1100 km s^{-1} and then decreases to about 800 km s^{-1}. Both the predicted arrival time and speed at the Earth are well confirmed by the in situ measurements. The gradual SEP events observed by three widely separated spacecraft show time profiles much more complicated than suggested by the standard conceptual picture of SEP event heliolongitude distribution. Evolving shock properties, the realistic time-dependent connection between the observer and shock source, and a possible role of particle perpendicular diffusion may be needed to interpret this SEP event spatial distribution.

Key words: shock waves – solar-terrestrial relations – solar wind – Sun: coronal mass ejections (CMEs) – Sun: particle emission – Sun: radio radiation

Online-only material: animations, color figures

1. INTRODUCTION

In the last three years we have witnessed a long solar minimum with the lowest level of solar activity in the space age. The Sun was extraordinarily quiet during this unusual minimum, for example, historically weak solar wind (e.g., McComas et al. 2008; Steinberg et al. 2010), low solar irradiance and radio flux, and effectively no sunspots. Some speculated that the current minimum might go on as the solar activity did not appear to pick up.

A spectacular coronal mass ejection (CME) occurred on 2010 April 3 and produced the largest, fastest interplanetary CME (ICME) at 1 AU since the 2006 December 13 event, indicative of awakening of the Sun from a long minimum. (Liu et al. 2008b provide a comprehensive description of the 2006 December 13 CME.) The 2010 April 3 event is associated with a B7.4 flare, significant EUV dimming and waves, radio bursts, a prominent shock wave, solar energetic particle (SEP) events, and a prolonged geomagnetic storm. The storm caused a communication failure with the *Galaxy 15* satellite at 09:48 UT on April 5, soon after the arrival of the shock at L1 (07:55 UT). A "Tiger Team" was formed at the National Oceanic and Atmospheric Administration (NOAA) to assess the space weather conditions at the time of the *Galaxy 15* satellite anomaly. Their report shows that, although moderate, the geomagnetic storm resulted in a remarkable increase in the local flux of energetic particles near *Galaxy 15*, which can cause surface and internal satellite charging (Denig et al. 2010).

Figure 1 shows the configuration of the planets and spacecraft in the ecliptic plane during the time of the CME. There are several spacecraft looking at the Sun including the *Solar and Heliospheric Observatory* (*SOHO*; Domingo et al. 1995) at L1 and the *Solar Terrestrial Relations Observatory* (*STEREO*; Kaiser et al. 2008) away from the Sun–Earth line. *STEREO* is comprised of two spacecraft with one preceding the Earth (*STEREO A*) and the other trailing behind (*STEREO B*). During the time of the CME, the two spacecraft are separated by about 138.°8 in longitude. Each of the *STEREO* spacecraft carries an identical imaging suite, the Sun Earth Connection Coronal and Heliospheric Investigation (SECCHI; Howard et al. 2008), which can image a CME from its birth in the corona all the way to the Earth and beyond. *STEREO* also has several sets of in situ instrumentation, including the In Situ Measurements of Particles and CME Transients package (Luhmann et al. 2008) and the Plasma and Suprathermal Ion Composition investigation (Galvin et al. 2008), which provide in situ measurements of the magnetic field, energetic particles, and the bulk solar wind plasma. At L1, *SOHO* gives another view of the Sun, and *ACE* and *WIND* monitor the near-Earth solar wind conditions, thus adding a third vantage point. Improved investigation of CME source evolution and interplanetary propagation is feasible with these multiple viewpoints. In particular, evolving CME properties determined from imaging observations can be compared with in situ measurements at 1 AU with the large field of view (FOV) of SECCHI.

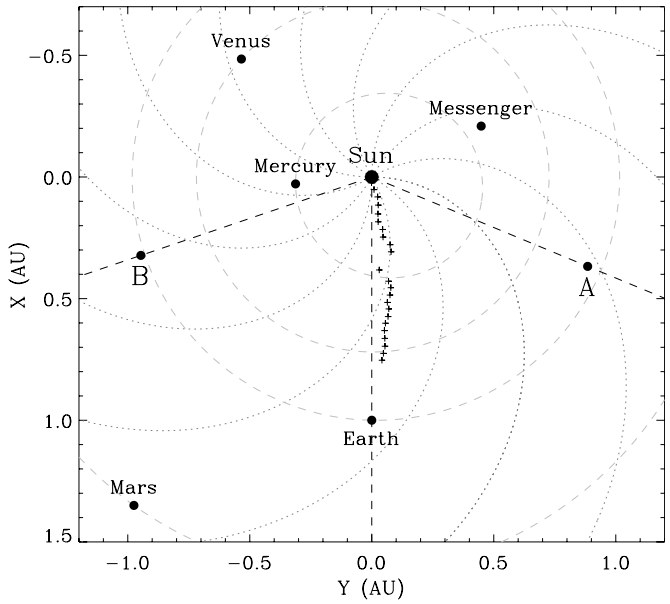

Figure 1. Positions of the spacecraft and planets in the ecliptic plane during the time of the CME. The gray dashed curves indicate the planetary orbits and the dotted lines show Parker spiral magnetic fields created with a solar wind speed of 450 km s^{-1}. The crosses mark the trajectory of the CME obtained from a triangulation technique. Saturn (not shown here) is about 12.°6 east of the Earth with a distance of 9.5 AU from the Sun.

Figure 1 also shows the CME trajectory determined from a geometric triangulation technique (see Section 3). The CME is propagating near the Sun–Earth line in the ecliptic plane. During the CME, Venus, Mercury, and the *Messenger* spacecraft orbiting Mercury are outside the space between *STEREO A* and *B*. Mars and Saturn are 1.65 AU and 9.5 AU away from the Sun and 35.°8 and 12.°6 east of the Earth, respectively. These planets experience space weather at the impact of CMEs or interplanetary shocks as the Earth does (e.g., Gurnett et al. 2002; Prange et al. 2004). A significant portion of the heliosphere would be disturbed by the 2010 April 3 event. During its propagation through the solar system, the CME is likely to have effects on Mars and Saturn as their longitudinal separations from the Earth are relatively small, but may not on Venus or Mercury. All the present planets have spacecraft making in situ measurements around them, which may be able to detect the interplanetary disturbances associated with the CME.

The 2010 April 3 event is also unique in several other aspects. It is the fastest and probably the biggest CME observed by both *STEREO A* and *B* through the whole Sun–Earth space up to the time of this writing. The longitudinal separation between the two spacecraft (138.°8) is much larger than those during other Earth-directed CMEs in the *STEREO* era (e.g., Liu et al. 2008c; Kilpua et al. 2009; Wood et al. 2009; Davis et al. 2009; Liu et al. 2010a, 2010b; Lugaz 2010; Farrugia et al. 2011). This provides a great opportunity to test the geometric triangulation technique for tracking CMEs proposed by Liu et al. (2010a), as we move from small, slow to large, fast events and from small to large longitudinal separations of the two spacecraft. The CME drives a strong shock visible in white-light images and finally observed in situ at the Earth, which generates gradual SEP events detected by three widely separated spacecraft at 1 AU (see Section 4). This presents the first opportunity to study the longitudinal distribution of gradual SEP events in the *STEREO* era. It is also a unique opportunity to make multipoint measurements of solar source signatures, CME/ICME properties, and the solar wind, thus providing a comprehensive temporal and spatial picture of a CME.

The 2010 April 3 event is of general interest to both the public and scientific community, given its occurrence at the end of an unusual solar minimum, association with a variety of solar and interplanetary signatures, a prolonged geomagnetic storm, and failure of a geosynchronous communications satellite. The purpose of this work is to study the solar source and heliospheric consequences of the CME in the frame of the Sun–Earth connection, combining remote sensing and in situ observations from a fleet of spacecraft. We examine solar source signatures in Section 2, CME interplanetary propagation in Section 3, and longitudinal distribution of the associated SEP events in Section 4. The results are summarized and discussed in Section 5. The present comprehensive view of the CME from the Sun far into interplanetary space provides a benchmark for today's studies of CMEs, associated phenomena, and space weather.

2. SOLAR SOURCE SIGNATURES

The CME originated from NOAA AR 11059 (S25°W03°). It is likely associated with an erupting filament, which leads to a classic B7.4 long-duration flare starting at 09:04 UT on April 3. Figure 2 displays running-difference images from the Extreme-ultraviolet Imaging Telescope (EIT) aboard *SOHO*. The most dramatic signature is a significant dimming around the active region, indicative of removal of the coronal plasma by the CME. The EUV dimming is not preceded by an obvious brightening, so there is no significant heating in the corona before the CME lifts off. This is consistent with a CME onset earlier than the flare (see Figure 4). Faint diffuse EUV brightenings, known as "EIT waves" (e.g., Neupert 1989; Thompson et al. 1998), are observed around the dimming and propagate across a large area of the solar disk. An accurate determination of the wave speed is not possible as the waves are very faint on the disk and the EIT cadence is low. Rising flare loops are seen when the EUV dimming has gone.

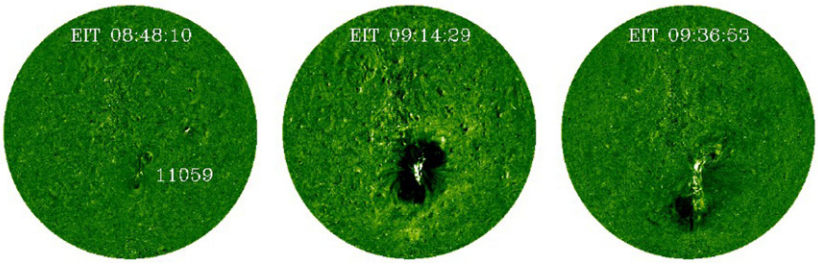

Figure 2. Running-difference images of EIT aboard *SOHO* at 195 Å showing the dimming and coronal waves associated with the CME.
(An animation and a color version of this figure are available in the online journal.)

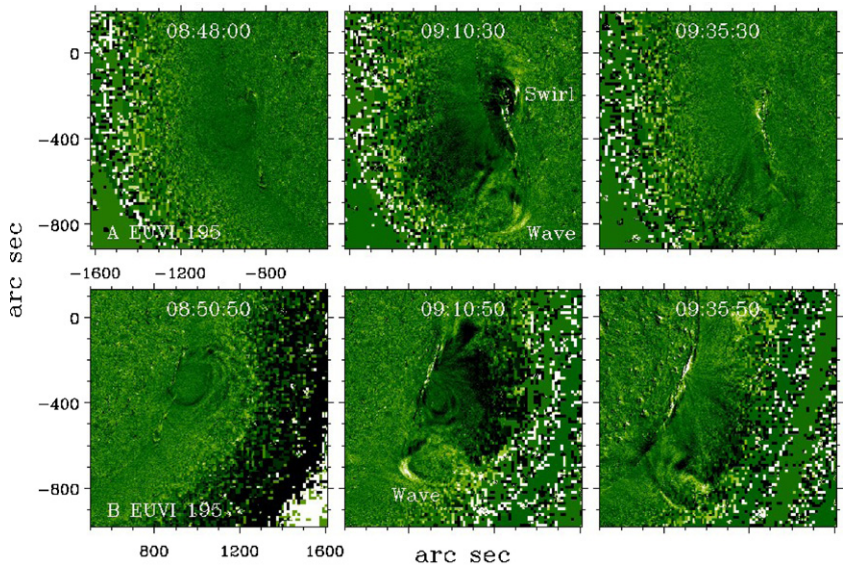

Figure 3. Running-difference images of EUVI aboard *STEREO A* (top) and *B* (bottom) at 195 Å showing the early CME evolution. The CME seems induced by a swirl motion at a footpoint. An EUV wave envelope is visible around the CME loop.

(Animations and a color version of this figure are available in the online journal.)

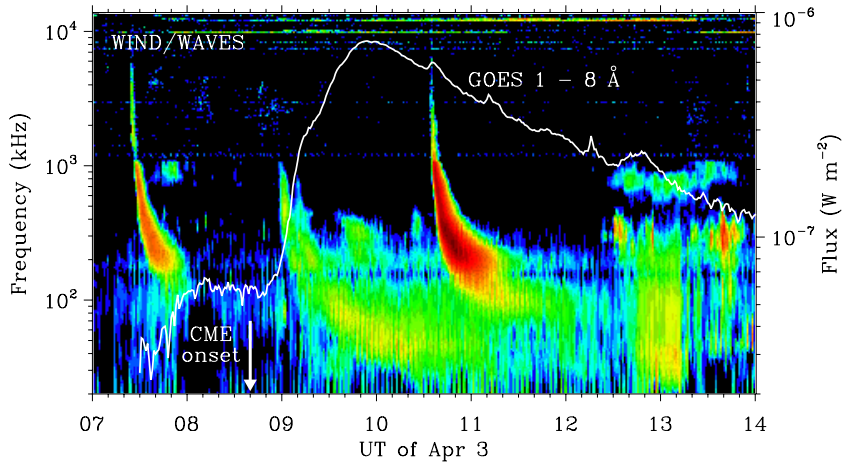

Figure 4. Dynamic spectrum (color shading) from *WIND*/WAVES and X-ray flux (solid line) from *GOES*. The vertical arrow shows the start time of the CME loop rise as observed by EUVI. Two type III bursts during the CME indicate particle injections at different times. There is no type II burst in the present frequency range although a CME-driven shock is observed (see Figure 6).

(A color version of this figure is available in the online journal.)

Figure 3 shows corresponding images from the Extreme-Ultraviolet Imager (EUVI) of SECCHI aboard *STEREO*. EUVI has an FOV similar to EIT but a higher cadence. The current cadence is 2.5 and 5 minutes for *STEREO A* and *B*, respectively, as compared with the nominal 12 minutes of EIT, so a better timing can be obtained. The CME is seen at the east limb of the Sun from *STEREO A* but at the west limb from *STEREO B*, as the longitudinal separation between the two spacecraft is 138°.8. This gives a great opportunity to look at the three-dimensional (3D) structure of the waves as well as the nascent CME. The CME seems to start from a pre-existing loop, better seen from *STEREO B*. The loop began to rise around 08:40 UT or earlier on April 3, which is at least 10 minutes before the flare impulsive phase (see Figure 4). The active region is a little inside the solar limb as viewed from *STEREO A*, so activities at the footpoints of the loop can be seen. The most striking feature is a swirl at the upper footpoint, which implies a strong shear in the magnetic field. The apparent vortex occurs at about the same time as the rise of the CME loop. The CME initiation may accompany this motion, which is more or less consistent with models that invoke shuffling of the magnetic field footpoints to launch a CME (e.g., Mikić & Linker 1994). The observed swirl appears to involve whole layers of the solar atmosphere and is apparently different from a pure displacement of the footpoints on the solar surface. Interestingly, the most significant coronal dimming occurs within the vortex, consistent with the idea that depletion of the coronal plasma is produced by stretching the magnetic field into interplanetary space.

The CME loop quickly expands with two ends still connected to the Sun. Associated with this intense expansion is a remote deflection of coronal structures, best visible at the south of the CME loop, which indicates a pressure wave running ahead of the CME. The deflected structures seem to match the latitudinal extent of the EUV waves observed on the disk by EIT. They also show a large vertical size as opposed to being confined in the low corona. A wave envelope likely forms all the way

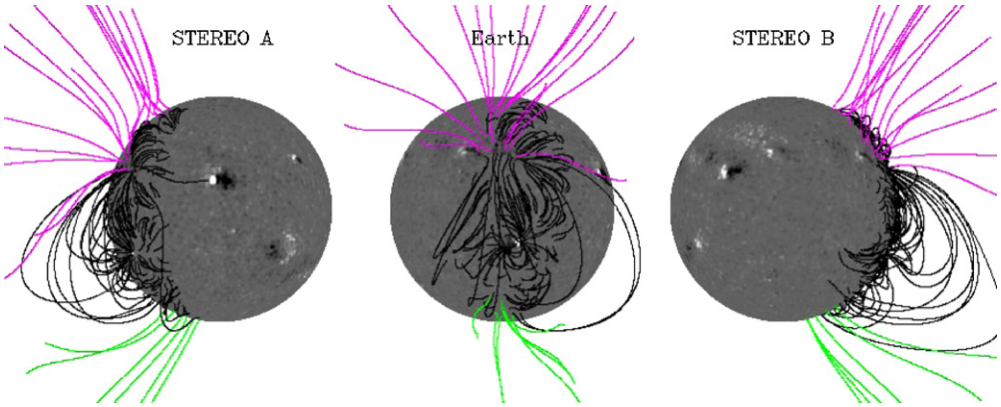

Figure 5. Coronal magnetic field topology around the active region on top of the photospheric field map as viewed from *STEREO A* (left), the Earth (middle), and *STEREO B* (right) on 2010 April 3. Closed field lines are drawn in black, and open field lines directed inward and outward are coded in green and pink, respectively. The active region is underneath the streamer belt (see also Figure 2).

(A color version of this figure is available in the online journal.)

around the CME loop. The EUV disturbances we see on the solar disk from EIT are just the low coronal part of the wave envelope or projections of the 3D wave structure against the solar disk. Apparently, the wave envelope is much wider than the CME loop, and it forms well after the eruption of the CME loop. Similar 3D structures of EUV waves have been observed by *STEREO* (Liu et al. 2009a; Patsourakos & Vourlidas 2009; Veronig et al. 2010). The observed wave envelope is reminiscent of a bow-shock signature driven by the CME, but without knowing the Alfvén speed in the ambient corona we cannot determine whether the wave has steepened into a shock. A CME-driven shock, however, exists in white-light images as suggested by a sharp edge all the way around the CME front (see Figure 6). Flare arcades develop after the CME has lifted off. These three-point observations indicate that the EUV wave is a magnetohydrodynamic (MHD) wave (presumably a fast mode), which may be the precursor of the shock seen in white light or the shock itself. It is also worth noting that the wave is a large-scale 3D structure rather than a horizontal disturbance as first inferred from EIT images. A better impression of the dimensionality of all the EUV features can be obtained from the online animations accompanying Figures 2 and 3.

Figure 4 displays the radio dynamic spectrum and the soft X-ray flux associated with the CME. Two type III radio bursts are observed during the event, one coincident with the flare impulsive phase and the other at the gradual phase, which indicate two separate injections of energetic particles. Type III bursts are produced by near-relativistic electrons. They drift downward rapidly in frequency and appear as almost vertical features in the dynamic spectrum. The first type III burst is relatively weak compared with the second one and does not have a high-frequency counterpart. It is not clear where the electrons producing the two type III bursts come from. Possible origins of the electrons include the flaring site, CME-driven shock, or magnetic field restructuring associated with the CME (e.g., Cane et al. 1981; Bougeret et al. 1998). There is no clear type II burst in the present frequency range. Type II bursts are remote signatures of a shock moving through the solar corona and heliosphere (e.g., Nelson & Melrose 1985; Cane et al. 1987). They also drift downward in frequency but much more slowly than type III bursts. Examination of ground-based spectrograph data also reveals no type II bursts in the metric domain. A CME-driven shock, however, may be present in white-light images (see Figure 6). Generation of type II bursts depends on the magnetic field and plasma conditions of the ambient medium, so even though a shock is present type II bursts might not appear. Also indicated in this figure is a CME onset time (08:40 UT) determined from EUVI observations. Here the CME onset is defined as the beginning of the rise of the CME EUV loop. The flare impulsive phase lags at least 10 minutes behind the CME onset.

Figure 5 shows three views of the coronal magnetic field configuration around the active region obtained with a potential-field source-surface model (e.g., Schatten et al. 1969; Altschuler & Newkirk 1969; Altschuler et al. 1977). Apparently, the source region is beneath the streamer belt. This is also indicated by a synoptic map with the whole streamer belt and open field lines. A direct consequence is that the CME has to disrupt the streamer belt as well as the heliospheric plasma sheet (HPS) on its way going out. The HPS is a layer around the heliospheric current sheet with increased mass density, which usually appears as a bright stalk at the tip of a helmet steamer in white-light images. A dent in the CME front is expected when the CME propagates through the HPS, provided that it expands on both sides of the HPS (e.g., Riley et al. 2003; Manchester et al. 2004; Liu et al. 2006). A similar dent structure in the preceding shock is also expected to form due to the interaction of the CME with the pre-existing HPS. Large-scale adjacent magnetic field loops, which connect the active region with coronal holes at the north and south, are observed underneath the streamer belt. As a result of this magnetic connection, the eruption of the CME would affect the coronal magnetic field configuration on a global scale (e.g., Liu et al. 2009b).

3. PROPAGATION IN INTERPLANETARY SPACE

After its eruption in the corona, the CME propagates into interplanetary space. CME evolution through the whole Sun–Earth space is imaged by SECCHI from both of the *STEREO* spacecraft. The CME is also observed in situ by *WIND* and *ACE* at 1 AU. We look at CME kinematics over a large distance and investigate how the imaging observations connect to the in situ signatures. A better understanding of the CME–ICME relationship can be achieved from this merged imaging and in situ study.

Figure 6 displays two synoptic views of the CME from *STEREO A* and *B*. In addition to EUVI, SECCHI also has two coronagraphs (COR1 and COR2) and two heliospheric imagers (HI1 and HI2). COR1 and COR2 have an FOV of 0.4–1° and

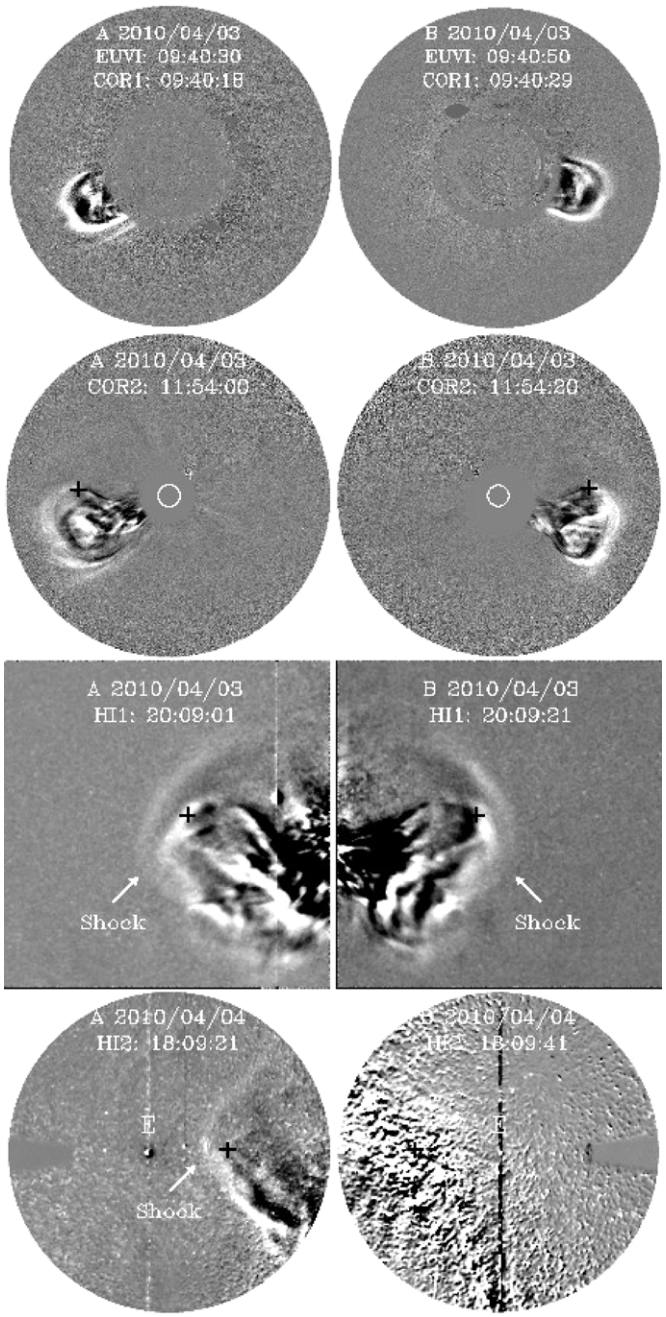

Figure 6. CME evolution (running-difference images) observed by *STEREO A* (left) and *B* (right) near simultaneously. The top row displays composite images of COR1 and EUVI at 195 Å and the bottom three rows show images from COR2, HI1, and HI2, respectively. The arrow indicates the CME-driven shock. The crosses mark the locations of a feature, which are obtained from the time–elongation maps (see Figure 7). The position of the Earth is labeled as E. The noise in HI2 of *STEREO B* is caused by the diffuse Milky Way.

(Animations of this figure are available in the online journal.)

0.°7–4° around the Sun, respectively. HI1 has a 20° square FOV centered at 14° elongation from the center of the Sun while HI2 has a 70° FOV centered at 53.°7. HI1 and HI2 can observe CMEs to the vicinity of the Earth and beyond by using sufficient baffling to eliminate stray light (Eyles et al. 2009). A panoramic view of the CME evolution from the corona all the way out to the Earth can be obtained from this figure and accompanying animations online. A smooth transition of the CME is observed through the whole imaging system of SECCHI. The CME rises as a typical three-part structure in COR1 and COR2, although it appears as a semicircular loop in EUVI. The CME shows a dimple in its front, presumably owing to the distortion by the pre-existing HPS that acts like an obstacle for CME propagation. The CME is flattened as well. The concave-outward structure becomes clearer in HI1. The observed structure is consistent with a CME source region below the helmet streamer (see Figure 5).

Of particular interest is a sharp edge all the way around the CME front in HI1, reminiscent of a bow shock produced by the CME. Later we will show by linking imaging observations with in situ signatures that the sharp white-light feature is likely the CME-driven shock. This feature is visible in both *STEREO A* and *B*, which indicates the exciting possibility to look at shock 3D structure and evolution in interplanetary space. The shock signature is also discernible in COR2 but much weaker. In HI2 it becomes much clearer and appears as a broad wave that sweeps over the inner heliosphere, while the driver itself is relatively weak and diffusive. In a separate paper we will address the idea that interplanetary shocks driven by CMEs are observable by heliospheric imagers. The rationale is that, as CMEs propagate in the interplanetary medium, the density within CMEs decreases to the ambient level or below because of expansion, so the most observable structure would be the sheath (a transition layer between the shock and CME front) due to shock compression. The shock front also has a dimple as expected (see Section 2). This concave-outward structure resulting from propagation through the HPS is consistent with MHD simulations (e.g., Odstrcil et al. 1996; Riley et al. 2003; Manchester et al. 2004) and in situ measurements (e.g., Burton et al. 1992; Liu et al. 2006).

The CME appears as a partial halo event in the Large Angle Spectroscopic Coronagraph (LASCO) C2 aboard *SOHO* (see http://umbra.nascom.nasa.gov/lasco/observations/halo/100403/). It forms a spectacular loop of dense material over the entire southern hemisphere. A closer look at the image of LASCO C2 around 10:33 UT on April 3 also reveals a weak edge ahead of the CME front, again suggesting the presence of a CME-driven shock. By 13:42 UT on April 3 it developed into a nearly complete halo in LASCO C3. The projected speed on the sky is about 512 km s^{-1} through C2 and C3, as measured along a position angle of 192° (counterclockwise from the north; K. Schenk 2010, private communication). This value is significantly smaller than the real speed (see Figure 8).

Figure 7 shows the time–elongation maps, which are produced by stacking the running-difference intensities of COR2, HI1, and HI2 within a slit of 64 pixels around the ecliptic plane (e.g., see Sheeley et al. 2008; Davies et al. 2009; Liu et al. 2010a). The CME gives rise to a track in the time–elongation maps, which exhibits a smooth transition through the FOVs of the cameras. The track can be identified up to about 60° elongation for *STEREO A* and about 40° for *STEREO B*. The CME signal in *STEREO B* is hampered by the intense emission from the Milky Way, although the time–elongation map can recover the signal to a substantial elongation. For comparison, the Earth is at an elongation angle of 58.°1 for *STEREO A* and 54.°4 for *STEREO B*. As can be seen from the maps, the CME is relatively isolated from other events, so contamination by or mixing with other events is probably not pronounced.

Elongation angles are extracted from the trailing edge of the track (the black/white boundary) where the contrast is the sharpest. The feature that is being tracked can be identified by plotting the extracted elongation angles over the images.

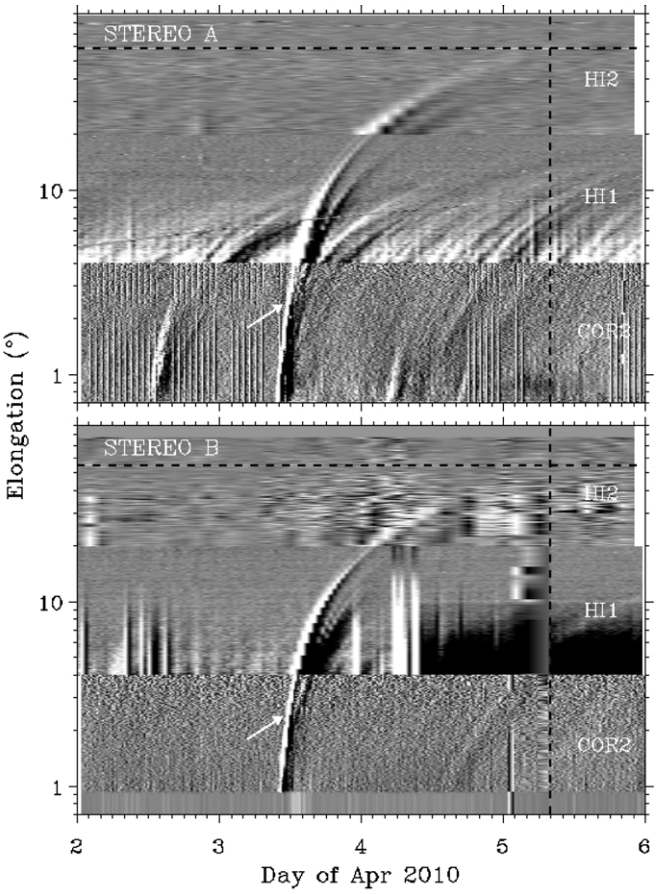

Figure 7. Time–elongation maps constructed from running-difference images of COR2, HI1, and HI2 along the ecliptic plane for *STEREO A* (upper) and *B* (lower). The arrow indicates a track associated with the CME. The vertical dashed line shows the arrival time of the CME-driven shock at the Earth and the horizontal dashed line marks the elongation angle of the Earth.

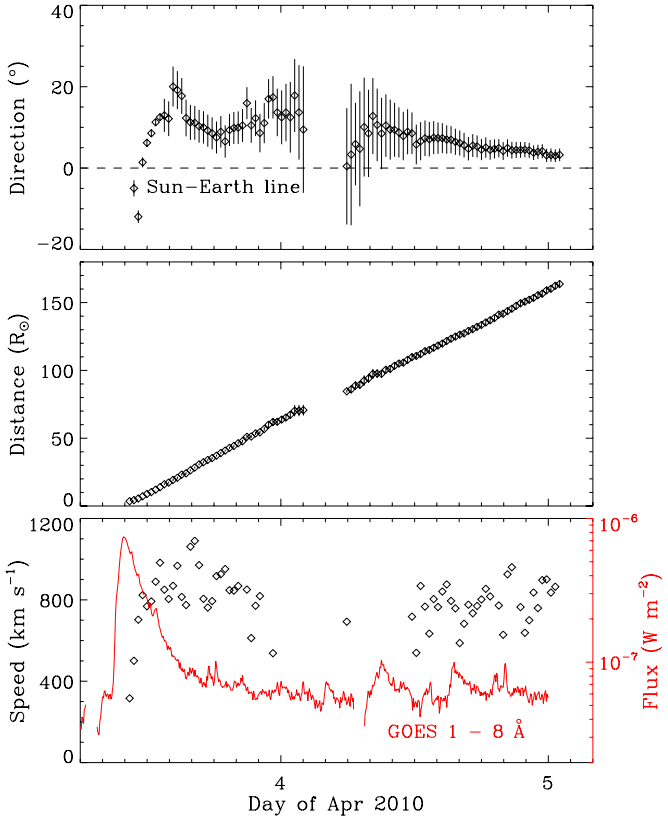

Figure 8. Propagation direction, radial distance, and speed of the CME leading edge derived from geometric triangulation. The dashed line indicates the Sun–Earth line. Error bars represent uncertainties mathematically derived from the measurements of elongation angles. The speeds are calculated from adjacent distances using a numerical differentiation with three-point Lagrangian interpolation. Overlaid on the speeds is the *GOES* X-ray flux (scaled by the red axis).

(A color version of this figure is available in the online journal.)

As illustrated in Figure 6, what is being tracked is likely the CME front (which has an enhanced density) in the ecliptic plane. The elongation angles are converted to radial distance and propagation direction using a geometric triangulation method developed by Liu et al. (2010a, 2010b). The basis of this technique is that the propagation direction and distance yield a certain elongation angle corresponding to the viewpoint. The two viewpoints from *STEREO* then form a simple geometry with which the propagation direction and radial distance can be derived. The method has no free parameters, so the solutions are unique. Liu et al. (2010a, 2010b) describe the mathematical formulas and detailed procedures used for reconstruction of those quantities.

The resulting CME kinematics in the ecliptic plane are displayed in Figure 8. The propagation direction is converted to an angle with respect to the Sun–Earth line. If the angle is positive (negative), the CME feature would be propagating west (east) of the Sun–Earth line in the ecliptic plane. The CME leading edge shows an indication of transition from eastward to westward at the early stage. After the westward transition the propagation direction stays around 10° west of the Sun–Earth line, although a slight tendency of moving eastward is observed at large distances. A track fitting approach (e.g., Sheeley et al. 2008) and coronagraph image forward modeling method (Thernisien et al. 2006) give a propagation angle of 9° and ±2° west of the Sun–Earth line, respectively (Möstl et al. 2010). Our results are consistent with these estimates. The westward motion seems coincident with CME acceleration (see the bottom panel). Similar results for other CMEs have been found by Liu et al. (2010b), who suggest that the westward motion is a universal feature for many CMEs at their acceleration phase. The rationale is that, when the motion of CMEs is dominated by the magnetic field connecting the Sun and ejecta, the magnetic field would produce a tendency for the ejecta to co-rotate with the Sun. The apparent co-rotation angle ($\geqslant$20°) seems larger than expected from pure angular momentum conservation. A possible explanation is that the CME brightness, which the triangulation technique relies on to determine the CME kinematics, may undergo quick changes in the inner corona due to interactions with the streamer belt, HPS, and other coronal structures nearby. The derived co-rotation angle is reduced to about 7° by comparing the relatively steady propagation angle (∼10°) with the solar source longitude (W03°). The change in the propagation angle may help to explain some observations, for example CMEs with solar source locations near the disk center miss the Earth, while those from the far eastern hemisphere of the Sun can hit the Earth (e.g., Wang et al. 2006).

The CME leading edge can be tracked out to 165 solar radii or 0.75 AU (without projection), a far more extensive region of the heliosphere than previously possible with coronagraph observations. Improved predictions of CME arrival time and speed at the Earth are expected given this continuous tracking

over a large distance. There is a data gap in the propagation angle and distance, which is due to singularities in the calculation scheme caused by the large spacecraft separation. The singularities might be avoided if a better calculation scheme can be employed for the triangulation technique. We calculate the speeds from adjacent distances using a numerical differentiation. Speeds derived this way usually have a considerable error bar, but they can show the variation with distance, which is very useful for probing CME interaction with the heliosphere. The accuracy of the speed can certainly be improved by fitting the distance overall. The variation information, however, would be lost. The speed first rises to 1000–1100 km s^{-1} and then decreases to about 800 km s^{-1}, presumably owing to interactions with the background heliosphere. The CME is still accelerating even after the flare maximum, as indicated by the timing with the *GOES* X-ray curve. Further acceleration after the flare maximum is not uncommon (e.g., Zhao et al. 2010; Chen & Kunkel 2010). Energy must be continuously fed into the CME even after the maximum heating and radiation have elapsed. Note that the deceleration largely occurs within a relatively short timescale, similar to other CMEs (Liu et al. 2010a, 2010b; Poomvises et al. 2010). Therefore, the maximum drag by the ambient medium should take place at distances not far from the Sun. Afterward the speed stays roughly constant around 800 km s^{-1}, which is likely the value measured in situ at 1 AU (see Figure 9).

Figure 9 shows an ICME identified from *WIND* in situ measurements based on the depressed proton temperature, smooth and strong magnetic field, and declining speed profile. A similar plasma and magnetic field structure is observed at *ACE*. A strong shock preceding the ICME, as can be seen from simultaneous increases in the plasma density, bulk speed, temperature, and magnetic field strength, passed the spacecraft at 07:55 UT on April 5. The radial width of the ICME (average speed times the duration) is about 0.37 AU. This is the largest, fastest ICME observed at 1 AU since the 2006 December 13 event. The ICME leading-edge speed is about 800 km s^{-1}, comparable to the counterpart of the 2006 December 13 event at 1 AU, whereas the near-Sun speed is much smaller (1100 km s^{-1} versus 2200 km s^{-1}). Apparently, deceleration of the 2010 April 3 event in interplanetary space is more moderate than the 2006 December 13 CME, which is consistent with the speed variation shown in Figure 8. The predicted arrival time of the CME leading edge, obtained by extrapolating the distances in Figure 8 with a second-order polynomial fit, lies right ahead of the ejecta and is coincident with a density-enhanced structure there. The arrival time prediction based on the triangulation technique agrees with the in situ measurements remarkably well. The predicted speed at 1 AU is about 790 km s^{-1} estimated by averaging the data points after April 4 in Figure 8, which is again well confirmed by the in situ data. It is remarkable that the geometric triangulation technique works very well given the vast longitudinal separation of the two spacecraft and the large CME size. A concern was that, for big CMEs like the present one, the structures seen by the two spacecraft may not be exactly the same. This concern is alleviated by the accuracy achieved by the triangulation technique. Liu et al. (2010a, 2010b) give a more detailed discussion of the effect of CME geometry on the triangulation analysis.

The association between imaging observations and in situ signatures can now be established. As shown earlier, the predicted arrival time of the CME front, which is the feature behind the shock-like signature in Figure 6, is coincident with a density-enhanced structure right ahead of the ejecta in the sheath

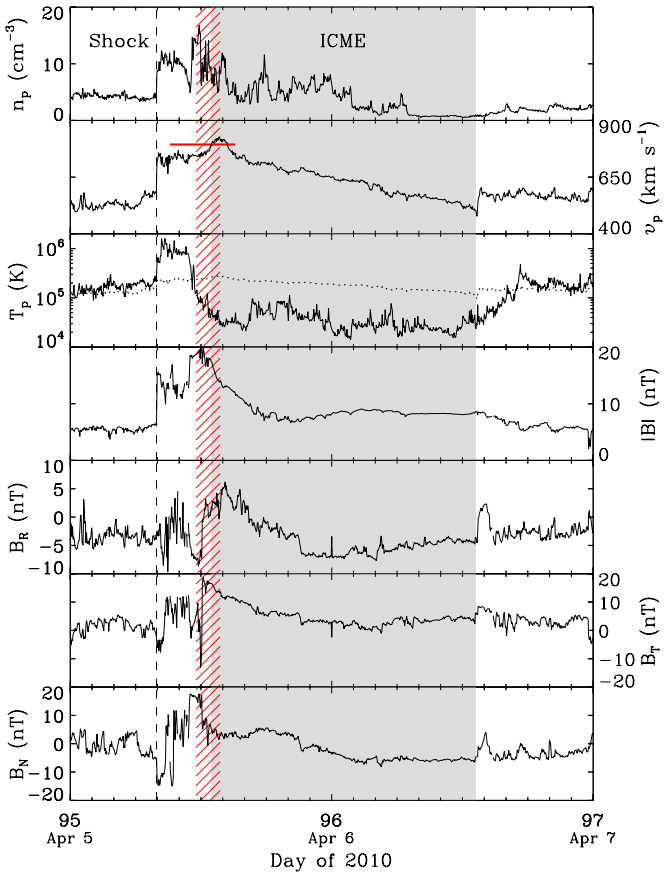

Figure 9. Solar wind plasma and magnetic field parameters across the ICME observed by *WIND*. From top to bottom, the panels show the proton density, bulk speed, proton temperature, and magnetic field strength and components, respectively. The shaded region indicates the ICME interval and the vertical dashed line marks the ICME-driven shock. The red hatched area shows the predicted arrival time (with uncertainties) of the CME leading edge and the horizontal line in the second panel marks the corresponding predicted speed at 1 AU. The dotted line denotes the expected proton temperature from the observed speed.

(A color version of this figure is available in the online journal.)

region (see Figure 9). This high-density structure from the in situ measurements is thus the CME front being tracked. This connection indicates that the white-light feature preceding the CME front in Figure 6 is the CME-driven shock, as the in situ measurements clearly show the presence of the shock ahead of the CME front (and the CME is fast enough to produce a shock). Note that identification of ICMEs from the solar wind is still a subjective undertaking. No universal standard can be used to identify ICMEs despite their various signatures in the solar wind. The comparison between imaging and in situ data indicates that the ejecta we usually identify (say, based on smooth, strong magnetic field) is likely the flux-rope part only. Liu et al. (2010a) also find, by linking imaging observations with in situ signatures, that a magnetic cloud identified from the solar wind only corresponds to the CME dark cavity. The actual ejecta interval may be larger if we take into account the high-density structures around the flux rope. The connection between imaging observations and in situ measurements is helpful for understanding the features seen in white light as well as ICME signatures observed in situ.

The magnetic field shown in Figure 9 has a prolonged negative (southward) component spanning the ICME and its trailing

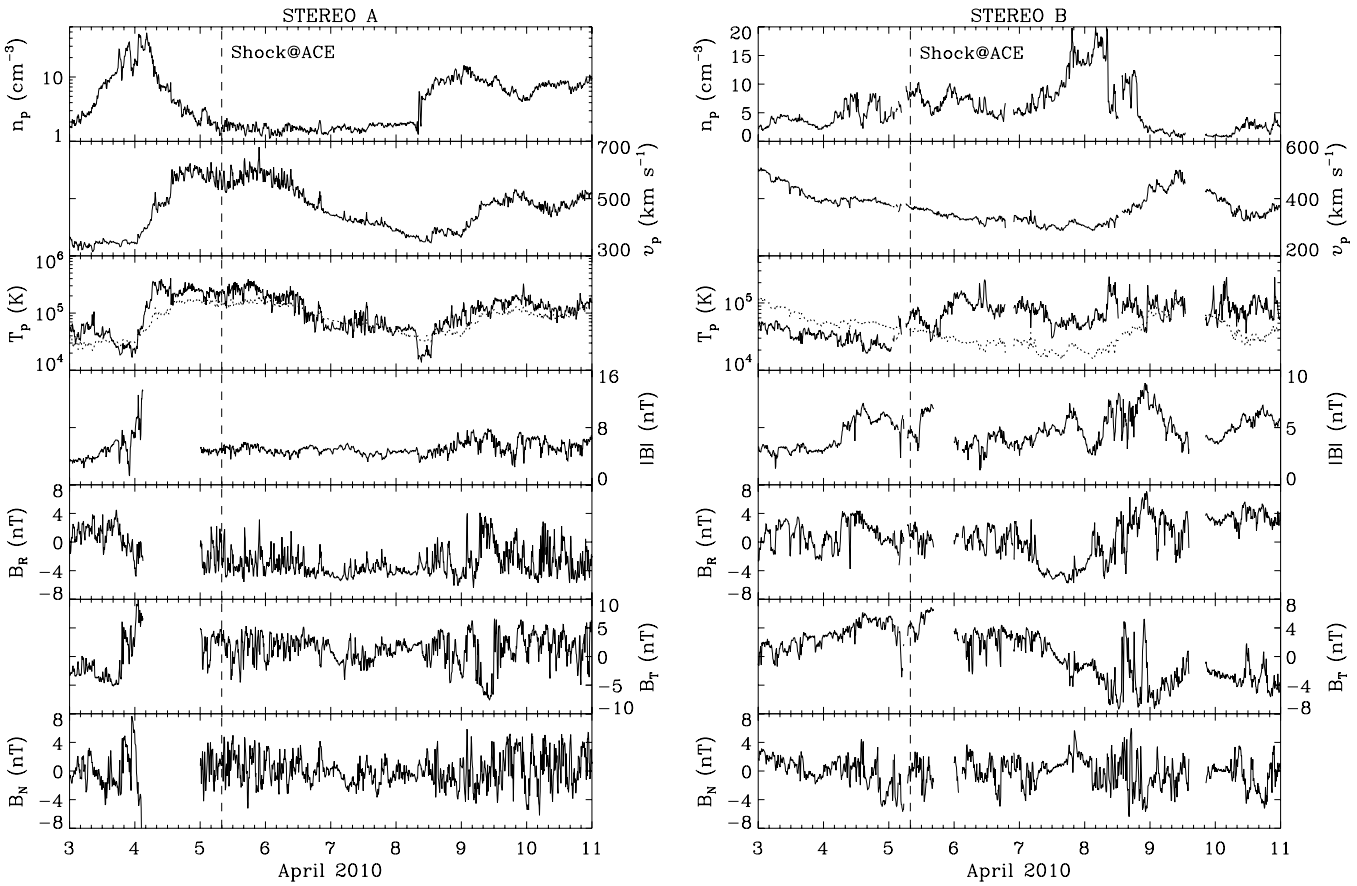

Figure 10. Same as Figure 9, but for the measurements at *STEREO A* (left) and *B* (right). Note that the vertical dashed line shows the shock arrival time at the Earth. Neither the ICME nor the shock is observed at the two spacecraft.

region. A southward magnetic field can reconnect with geomagnetic fields and thus is a key factor in producing geomagnetic storms (Dungey 1961; Gosling et al. 1991). The D_{st} index, a measure of the severity of geomagnetic storms (the more negative, the more intense), has a minimum value of about −72 nT for the present case (Möstl et al. 2010). Although moderate, the geomagnetic storm caused a breakdown of the *Galaxy 15* satellite for more than half a year (http://www.space.com/9677-galaxy15-zombie-satellite-life.html). Also note a strong southward magnetic field component in the sheath region right behind the shock. It is this short interval that accounts for the commencement of the geomagnetic storm. The southward magnetic field in this interval is likely produced by the non-radial deflection flows downstream of the shock (Liu et al. 2008a).

Figure 10 displays the solar wind data from *STEREO A* and *B* for an interval of 8 days. No obvious ICME signatures are observed during this time period, such as depressed proton temperature and smooth, strong magnetic field. The shock is not observed either. It is likely that the ICME as well as the shock misses the two spacecraft. This seems reasonable given the CME propagation direction near the Sun–Earth line in the ecliptic plane and a large longitudinal separation between *STEREO A* and *B* (138.°8). The ICME may also have been so well assimilated into the ambient structures that it is no longer recognizable at its flanks. Note a stream interaction region observed by *STEREO A* around April 4. The proton density, temperature, and magnetic field strength are enhanced when a fast stream overtakes a slow one. This stream interaction region may have effects on particle transport (see Figure 13).

As shown in Figure 1, the 2010 April 3 event may cause interplanetary disturbances detectable at Mars and Saturn since their longitudinal separations from the Earth are relatively small. Here we propagate the solar wind disturbance outward from the Earth using an MHD model, in an effort to make predictions that may be compared with the in situ measurements beyond 1 AU. The model assumes spherical symmetry and has had success in connecting solar wind observations at different spacecraft (e.g., Wang et al. 2001; Richardson et al. 2005, 2006; Liu et al. 2006). All physical quantities at the inner boundary (1 AU) are set to the average near-Earth solar wind conditions. The MHD equations are then solved to give a steady-state solar wind solution. Solar wind measurements at the Earth (an interval of 100 days containing the ICME data) are introduced into the model as perturbations. We then follow the perturbations outward from the model output. Figure 11 shows the evolution of solar wind stream structures from the Earth all the way to Saturn. The shock persists out to Mars (1.65 AU) but then appears smoothed out due to stream interactions. The streams around the ICME at the Earth develop into two separate ones, both of which appear steepened into shocks later. The predicted arrival time of the CME-driven shock at Mars is about 15:50 UT on April 6, while Saturn would encounter a shock-like stream around 12:14 UT on April 29. Note that the shock may have already lost its identify at Saturn because of stream interactions. We leave these predictions for future possible comparison with

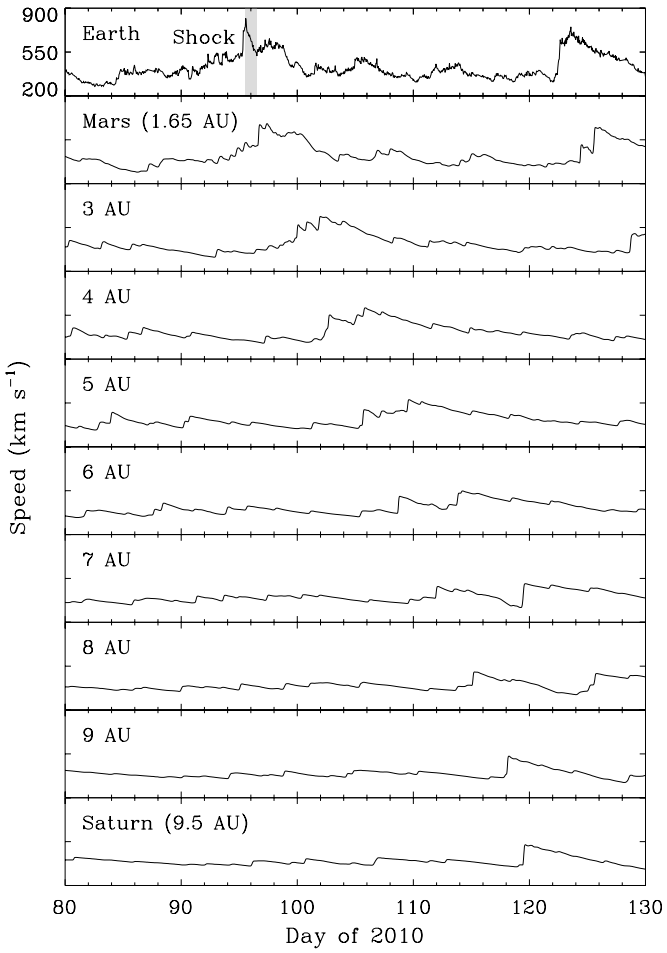

Figure 11. Evolution of solar wind speeds from the Earth to Saturn via the MHD model. The shaded region represents the ICME interval at the Earth. The curve in the top panel is the observed speed at *WIND*, and others are predicted speeds at given distances.

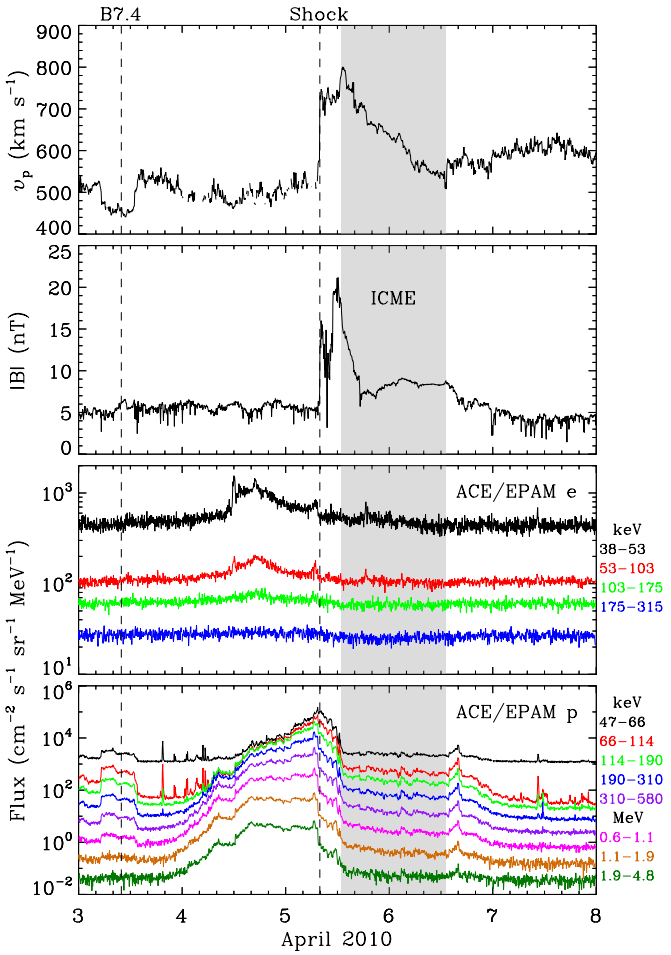

Figure 12. Solar wind speed, magnetic field strength, and intensities of electrons and protons at different energy channels measured by *ACE*. The ICME interval is indicated by the shaded region. The times of the flare and shock arrival at the Earth are marked by the vertical dashed lines.

(A color version of this figure is available in the online journal.)

in situ measurements at the planets (say, from *Cassini* around Saturn).

4. LONGITUDINAL DISTRIBUTION OF SEP EVENTS

CME-driven shocks are responsible for the most intense SEP events, often referred to as gradual events due to their long duration (up to several days). Currently, the longitudinal distribution of gradual SEP events with respect to a CME location is understood from the generally spiral nature of the interplanetary magnetic field, which produces a time-dependent connection between an observer and the moving shock (Cane et al. 1988; Reames 1999). Due to the spiral magnetic field, an observer's connection point to the shock swings eastward as the shock propagates outward. It is assumed that particle intensities peak near the nose of the shock and decline on the flanks. The observed particle intensities would change with time according to the connection point, resulting in three main categories of gradual SEP time profiles. Refer to Figure 3.4 of Reames (1999) for details. The 2010 April 3 event provides the first opportunity in solar cycle 24 to test this conceptual picture with three widely separated spacecraft. Multipoint observations of the CME properties over a large distance also give an unprecedented opportunity to make proper description of the SEP events and their relationship to the CME.

Figure 12 shows the particle intensities measured by the Electron, Proton, and Alpha Monitor (EPAM) of *ACE* together with the solar wind speed and magnetic field strength. The proton intensities are clearly enhanced near the CME-driven shock. The shock should be producing energetic particles throughout the interplanetary transit. It continues to accelerate protons to ~MeV energies at 1 AU. The protons show a clear velocity dispersion, with the highest energy particles arriving first. The particles observed before the shock arrival are emitted by the shock when it is still close to the Sun, and the fastest ones win the race to reach the observer. The protons that peak near the shock are known as energetic storm particle (ESP) events, which are thought to be shock-accelerated particles trapped by the magnetic field fluctuations around the shock (e.g., Lee 1983). There is an apparent exclusion of the protons from the ICME interior, as if its magnetic field forms a barrier for their entry into the ejecta. The electrons show an apparently different profile. They seem to peak before the shock passage, and only a slight enhancement is observed near the shock. These features are similar to the gradual SEP event during the 2006 December 13 CME (Liu et al. 2008b). There is no obvious particle enhancement associated with the B7.4 flare.

The observed proton time profiles are consistent with the idealized picture described by Cane et al. (1988) and Reames

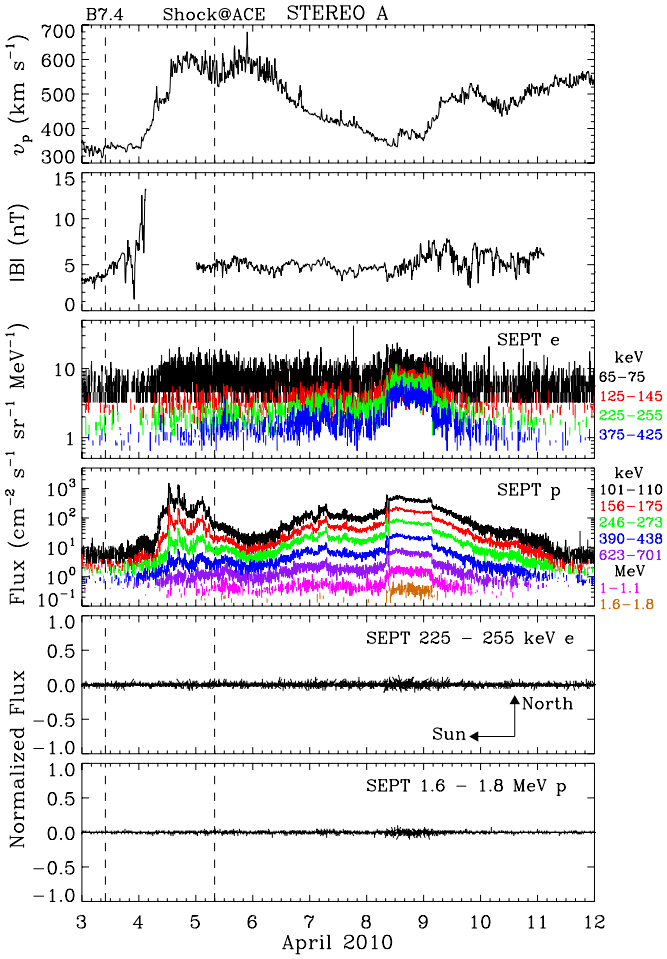

Figure 13. Same as Figure 12, but for the measurements at *STEREO A*. Also shown are the anisotropies of electrons and protons observed by SEPT aboard *STEREO A*. The solid lines in the two bottom panels denote the normalized intensity differences along the directions defined by the arrows in the fifth panel. Anisotropy information can be obtained if the particle intensity has an excess along a certain direction.

(A color version of this figure is available in the online journal.)

(1999). Our triangulation analysis of the imaging observations shows that the CME is headed toward the Earth in the ecliptic plane. When the shock is still near the Sun, *ACE* is connected to the western flank of the shock by the spiral interplanetary magnetic field. Later, when the shock is near the Earth, *ACE* will be connected to the nose of the shock. It is assumed that particle acceleration is strongest at the nose of the shock and declines toward the flanks. Therefore, *ACE* should see a slow initial rise in the proton intensity early in the event, and later it would observe a peak in the time profiles corresponding to the ESP event as the shock reaches 1 AU. When *ACE* crosses into the CME, proton intensities will decrease, presumably due to the closed strong magnetic fields within the ejecta. This is generally what the observations have shown.

Corresponding data from *STEREO A* are shown in Figure 13. Note that neither the shock nor ICME is observed at *STEREO A*. The proton intensities show a complex time profile, with one enhancement peaking before the shock passage at the Earth and the other one about 3 days behind the shock passage. The first enhancement has several spikes, indicative of either a complicated magnetic connection between the spacecraft and shock or an irregular shock structure. The electron time profiles are noisy, but two bumps coincident with the proton enhancements can be recognized. The second particle enhancement is not observed at *ACE* during the same time period. Both of the particle enhancements are likely associated with the shock. *STEREO A* is on the western side of the CME, and it should be connected to the far western flank of the shock by the interplanetary magnetic field when the shock is close to the Sun. The spacecraft would thus see slowly increasing intensities as its connection point swings eastward toward the nose of the shock. Peak intensities or flat time profiles corresponding to nearly constant acceleration, however, only occur after the shock has well passed 1 AU, where field lines connect the spacecraft to the nose of the shock from behind. The observed proton time profiles agree roughly with the conceptual picture of Cane et al. (1988) and Reames (1999), although deviations are observed (e.g., the rapid rise of the proton intensity in the first enhancement). Note that the second enhancement is about 3 days behind the shock arrival at 1 AU. At that time, the shock may have already reached 2 AU given the observed speed at 1 AU (see Figure 11). Also note that the shock strength may weaken as it travels outward.

The two bottom panels in Figure 13 show anisotropy information of the particles provided by the Solar Electron and Proton Telescope (SEPT). SEPT has two separate telescopes, one looking in the ecliptic plane along the nominal Parker spiral field toward and away from the Sun and the other looking vertical to the plane toward the south and north, respectively (Müller-Mellin et al. 2008). The lines in the two panels represent the intensity differences along the directions for each telescope, i.e., differences between the south and north and between the two opposite directions along the Parker field. The intensity difference is normalized by 150 cm^{-2} s^{-1} sr^{-1} MeV^{-1} for the electrons and 20 cm^{-2} s^{-1} sr^{-1} MeV^{-1} for the protons. The particles seem isotropic according to the intensity differences. The stream interaction region around April 4 (also see Figure 10, left) may disturb the magnetic field connection between *STEREO A* and the shock source and/or scatter the particles toward isotropy. This may help explain the particle time profiles observed at *STEREO A*.

Figure 14 displays the particle data from *STEREO B*. Again, neither the shock nor ICME is observed at the spacecraft. The proton time profiles are even more complex compared with the observations of *STEREO A*, with two peaks bracketing the shock passage at the Earth and several others behind. These peaks are likely associated with the 2010 April 3 CME as it is relatively isolated, although contributions from other heliospheric transients cannot be excluded completely. The electron intensities have a main peak before the shock arrival at the Earth and then decline. *STEREO B* is on the eastern side of the CME. The spacecraft can be well connected to the nose of the shock when the shock is still near the Sun. Then the connection point moves eastward toward the far eastern flank as the shock propagates outward. According to the classic picture of Cane et al. (1988) and Reames (1999), the spacecraft would see a prompt initial rise in the particle intensity and then a decline over a long time. The observed electron time profiles are more or less consistent with this view, but the proton profiles are much more complicated. Again, the magnetic connection between the spacecraft and shock may not be as simple as imagined, and the shock may have an irregular structure as well as an evolving strength. Anisotropy information of the particles is also shown in Figure 14. The intensity differences are normalized by the same factors as in Figure 13. An apparent anisotropic distribution is observed in both the electrons and

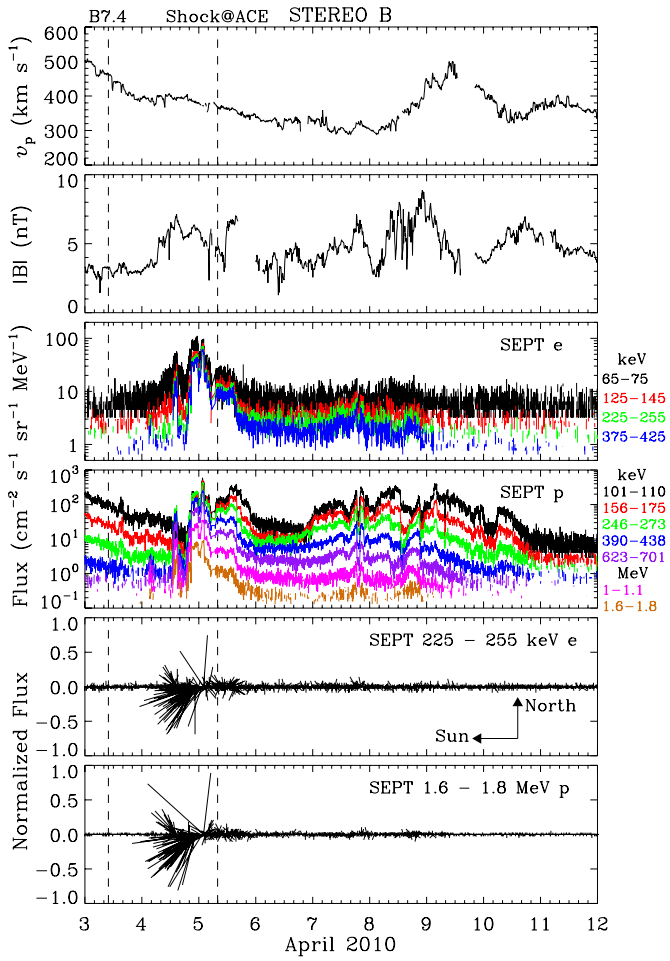

Figure 14. Same as Figure 13, but for the measurements at *STEREO B*. Particles before the shock arrival at the Earth have an excess in the sunward and southward directions.

(A color version of this figure is available in the online journal.)

protons before the shock arrival at the Earth. They are moving largely sunward and southward. This may indicate deflection by magnetic mirroring or a complex magnetic connection between the spacecraft and shock source.

The above results show that the organization of gradual SEP event time profiles relative to CME location is in some respects consistent with but also much more complicated than the currently held view developed by Cane et al. (1988) and Reames (1999). The interplanetary magnetic field, which connects an observer with the shock source, is not as simple as a generally spiral pattern. Proper interpretation of the time-dependent connection between the observer and shock requires knowledge of the ambient heliospheric conditions as well as the prevailing large-scale 3D structure that may perturb the magnetic field topology (e.g., Luhmann et al. 2007, 2010). Evolving shock properties (e.g., strength and irregular structure) as a function of distance should also be taken into account. Finally, particle scattering and diffusion across magnetic field lines may also play a role in the spatial distribution of this SEP event.

5. SUMMARY AND DISCUSSION

We have investigated the solar source and heliospheric consequences of the 2010 April 3 CME, combining remote sensing and in situ observations from a fleet of spacecraft. The CME has caused the largest, fastest ICME at 1 AU since the 2006 December 13 event, the first gradual SEP events distributed over wide longitudes in solar cycle 24, and a prolonged geomagnetic storm that resulted in a breakdown of the *Galaxy 15* satellite. Several periods of intense solar activities have followed at the time of this writing, including 2010 August and 2011 February when the first X-class flare in solar cycle 24 occurred. Apparently, the Sun has awakened from a long, deep minimum.

The CME originated from a source region (AR 11059) beneath the streamer belt. It is associated with a B7.4 long-duration flare, significant coronal dimming, EUV waves, and Type III radio bursts. The CME initiation is accompanied by a whirling motion at one of the footpoints, which appears to involve whole layers of the solar atmosphere. Depletion of the coronal plasma by the ejection gives rise to a dramatic dimming around the active region. The rise of the CME EUV loop occurs at least 10 minutes before the flare impulsive phase, consistent with the fact that no obvious coronal brightening is observed before the dimming. The CME also generates coronal waves, known as "EIT waves," which show a large-scale 3D structure as viewed from three widely separated spacecraft. They appear as horizontal disturbances on the solar disk but actually form an envelope around the CME as seen from the limb. They produce a remote deflection of coronal structures, indicating a nature of pressure waves running ahead of the CME. These multipoint observations suggest that the EUV wave is an MHD wave, which may be the precursor of the CME-driven shock or the shock itself in the present case. These results hold important clues for understanding CME initiation and associated solar signatures.

The CME and its preceding shock are imaged by both *STEREO A* and *B* almost throughout the whole Sun–Earth space. A dent is observed in the CME front as well as the shock, probably resulting from interaction with the pre-existing HPS after the CME has disrupted the streamer belt from below. The observed concave-outward structure is consistent with previous observations and simulations (e.g., Burton et al. 1992; Odstrcil et al. 1996; Riley et al. 2003; Manchester et al. 2004; Liu et al. 2006). The CME manifests as an ICME with a forward shock from in situ measurements at the Earth, but perhaps the ICME and shock miss *STEREO A* and *B*. The CME kinematics determined from a geometric triangulation technique (Liu et al. 2010a, 2010b) agree with the near-Earth in situ measurements remarkably well. Both the predicted arrival time and speed at the Earth are well confirmed by the in situ data. Again, this proves the efficacy of the triangulation technique for a variety of CMEs (from small, slow to large, fast) and a wide range of spacecraft longitudinal separations (see also Liu et al. 2010a, 2010b). Note that 1 AU speed predictions from other methods usually have a large uncertainty, whereas the triangulation technique can pin down the speed to within several tens of km s^{-1} as shown by comparison with in situ data. The longitudinal separation between *STEREO A* and *B* in the present case (138.°8) is comparable to the separation between L4 and L5. The success of the technique demonstrates the feasibility of the triangulation concept proposed by Liu et al. (2010b), which places dedicated spacecraft at L4 and L5 to make routine observations for real-time space weather forecasting.

CME kinematics in the ecliptic plane are obtained as a function of distance out to 0.75 AU by the triangulation technique. The CME propagation direction shows a transition

from eastward to westward at the early stage, similar to other events (Liu et al. 2010b), and then stays around 10° west of the Sun–Earth line with a slight tendency of moving eastward at large distances. The westward motion may result from the dominance early in the event by the magnetic field that connects the Sun and ejecta, as suggested by Liu et al. (2010b). The speed of the CME first increases to 1000–1100 km s^{-1} and then decreases to about 800 km s^{-1}. The deceleration, presumably due to interactions with the ambient solar wind, mainly occurs within a relatively short timescale, which is also true for other CMEs (Liu et al. 2010a, 2010b; Poomvises et al. 2010). Comparison with the 2006 December 13 event indicates that, for CMEs faster than the solar wind, the larger the speed, the more rapid the deceleration. The kinematics over an extensive region are important for understanding CME interaction with the heliosphere. A better understanding of the CME–ICME relationship is also achieved by tracking the CME over such a large distance. Connection between imaging observations and in situ measurements suggests that the white-light feature preceding the CME front is the CME-driven shock. It indicates that a magnetic cloud identified from the solar wind is usually only part of the ejecta seen in white light. Propagation of the solar wind disturbance beyond 1 AU is investigated with an MHD model, in order to make predictions on CME impact on other planets outside 1 AU. The model predicts that the CME-driven shock could arrive at Mars at about 15:50 UT on April 6 and Saturn may see a shock-like stream around 12:14 UT on April 29.

The CME-driven shock produces gradual SEP events observed at three widely separated spacecraft, which provides the first opportunity in solar cycle 24 to test the currently held view of gradual SEP event distribution (Cane et al. 1988; Reames 1999). *ACE*, which is near the CME propagation direction in the ecliptic plane, observes a slow initial rise in the proton intensity early in the event and later peaked profiles corresponding to the ESP event as the shock reaches 1 AU. This is consistent with the time-dependent connection between *ACE* and the shock source by the interplanetary magnetic field, which swings from the western flank of the shock to the nose during CME transit from the Sun to 1 AU. Proton intensities decrease as *ACE* crosses into the ejecta, where the magnetic field lines may form a barrier against particle entry. *STEREO A* is on the western side of the CME and observes complex SEP time profiles with two main enhancements separated by about 3 days. The second enhancement with flat time profiles likely occurs when field lines connect the spacecraft to the nose of the shock from behind (i.e., the shock has already passed 1 AU). *STEREO B* is on the eastern side of the CME and the observed SEP time profiles are even more complex. The particles observed at *STEREO A* seem isotropic, whereas those observed at *STEREO B* are apparently anisotropic. The observations at the two *STEREO* spacecraft are not quite consistent with the gradual SEP event distribution relative to CME location purely organized by the spiral magnetic fields. Evolving shock properties (e.g., strength and structure) and realistic time-dependent connection between the observer and shock with a possible role of particle diffusion must be taken into account. This would require knowledge of the ambient heliospheric conditions as well as the prevailing large-scale 3D structure relevant to particle production and magnetic field connection.

The research was supported by the *STEREO* project under grant NAS5-03131. SECCHI was developed by a consortium of NRL, LMSAL and GSFC (US), RAL and University of Birmingham (UK), MPI (Germany), CSL (Belgium), and IOTA and IAS (France). We also acknowledge the use of data from *WIND*, *ACE*, *SOHO*, and *GOES*. R. Lin has been supported in part by the WCU grant (no. R31-10016) funded by KMEST.

REFERENCES

Altschuler, M. D., Levine, R. H., Stix, M., & Harvey, J. 1977, Sol. Phys., 51, 345
Altschuler, M. D., & Newkirk, G. 1969, Sol. Phys., 9, 131
Bougeret, J.-L., et al. 1998, Geophys. Res. Lett., 25, 2513
Burton, M. E., Siscoe, G. L., & Smith, E. J. 1992, J. Geophys. Res., 97, 12283
Cane, H. V., Reames, D. V., & von Rosenvinge, T. T. 1988, J. Geophys. Res., 93, 9555
Cane, H. V., Sheeley, N. R., Jr., & Howard, R. A. 1987, J. Geophys. Res., 92, 9869
Cane, H. V., et al. 1981, Geophys. Res. Lett., 8, 1285
Chen, J., & Kunkel, V. 2010, ApJ, 717, 1105
Davis, C. J., Davies, J. A., Lockwood, M., Rouillard, A. P., Eyles, C. J., & Harrison, R. A. 2009, Geophys. Res. Lett., 36, L08102
Davies, J. A., et al. 2009, Geophys. Res. Lett., 36, L02102
Denig, W. F., et al. 2010, AGU Fall Meeting, abstract SH31D-03
Domingo, V., Fleck, B., & Poland, A. I. 1995, Sol. Phys., 162, 1
Dungey, J. W. 1961, Phys. Rev. Lett., 6, 47
Eyles, C. J., et al. 2009, Sol. Phys., 254, 387
Farrugia, C. J., et al. 2011, J. Atmos. Solar-Terr. Phys., in press
Galvin, A. B., et al. 2008, Space Sci. Rev., 136, 437
Gosling, J. T., McComas, D. J., Philips, J. L., & Bame, S. J. 1991, J. Geophys. Res., 96, 7831
Gurnett, D. A., et al. 2002, Nature, 415, 985
Howard, R. A., et al. 2008, Space Sci. Rev., 136, 67
Kaiser, M. L., Kucera, T. A., Davila, J. M., St. Cyr, O. C., Guhathakurta, M., & Christian, E. 2008, Space Sci. Rev., 136, 5
Kilpua, K. E. J., et al. 2009, Sol. Phys., 254, 325
Lee, M. A. 1983, J. Geophys. Res., 88, 6109
Liu, Y., Davies, J. A., Luhmann, J. G., Vourlidas, A., Bale, S. D., & Lin, R. P. 2010a, ApJ, 710, L82
Liu, Y., Luhmann, J. G., Bale, S. D., & Lin, R. P. 2009a, ApJ, 691, L151
Liu, Y., Luhmann, J. G., Lin, R. P., Bale, S. D., Vourlidas, A., & Petrie, G. J. D. 2009b, ApJ, 698, L51
Liu, Y., Manchester, W. B., Richardson, J. D., Luhmann, J. G., Lin, R. P., & Bale, S. D. 2008a, J. Geophys. Res., 113, A00B03
Liu, Y., Richardson, J. D., Belcher, J. W., Wang, C., Hu, Q., & Kasper, J. C. 2006, J. Geophys. Res., 111, A12S03
Liu, Y., Thernisien, A., Luhmann, J. G., Vourlidas, A., Davies, J. A., Lin, R. P., & Bale, S. D. 2010b, ApJ, 722, 1762
Liu, Y., et al. 2008b, ApJ, 689, 563
Liu, Y., et al. 2008c, ApJ, 677, L133
Lugaz, N. 2010, Sol. Phys., 267, 411
Luhmann, J. G., Ledvina, S. A., Krauss-Varban, D., Odstrcil, D., & Riley, P. 2007, Adv. Space Res., 40, 295
Luhmann, J. G., Ledvina, S. A., Odstrcil, D., Owens, M. J., Zhao, X.-P., Liu, Y., & Riley, P. 2010, Adv. Space Res., 46, 1
Luhmann, J. G., et al. 2008, Space Sci. Rev., 136, 117
Manchester, W. B. IV, et al. 2004, J. Geophys. Res., 109, A02107
McComas, D. J., et al. 2008, Geophys. Res. Lett., 35, L18103
Mikić, Z., & Linker, J. A. 1994, ApJ, 430, 898
Möstl, C., et al. 2010, Geophys. Res. Lett., 37, L24103
Müller-Mellin, R., et al. 2008, Space Sci. Rev., 136, 363
Nelson, G. J., & Melrose, D. B. 1985, in Solar Radiophysics: Studies of Emission from the Sun at Metre Wavelengths, ed. D. J. McLean & N. R. Labrum (Cambridge: Cambridge Univ. Press), 333
Neupert, W. M. 1989, ApJ, 344, 504
Odstrcil, D., Dryer, M., & Smith, Z. 1996, J. Geophys. Res., 101, 19973
Patsourakos, S., & Vourlidas, A. 2009, ApJ, 700, L182
Poomvises, W., Zhang, J., & Olmedo, O. 2010, ApJ, 717, L159
Prange, R., et al. 2004, Nature, 432, 78
Reames, D. V. 1999, Space Sci. Rev., 90, 413
Richardson, J. D., Wang, C., Kasper, J. C., & Liu, Y. 2005, Geophys. Res. Lett., 32, L03S03
Richardson, J. D., et al. 2006, Geophys. Res. Lett., 33, L23107
Riley, P., et al. 2003, J. Geophys. Res., 108, 1272
Schatten, K. H., Wilcox, J. M., & Ness, N. F. 1969, Sol. Phys., 6, 442

Sheeley, N. R., et al. 2008, ApJ, 675, 853
Steinberg, J. T., Skoug, R. M., Ryland, P., Kasper, J. C., Maruca, B. A., & Lepri, S. T. 2010, AGU Fall Meeting, abstract SH11B-1670
Thernisien, A. F. R., Howard, R. A., & Vourlidas, A. 2006, ApJ, 652, 763
Thompson, B. J., et al. 1998, Geophys. Res. Lett., 25, 2465
Veronig, A. M., Muhr, N., Kienreich, I. W., Temmer, M., & Vrsnak, B. 2010, ApJ, 716, L57
Wang, C., Richardson, J. D., & Paularena, K. I. 2001, J. Geophys. Res., 106, 13007
Wang, Y., Xue, X., Shen, C., Ye, P., Wang, S., & Zhang, J. 2006, ApJ, 646, 625
Wood, B. E., Howard, R. A., Plunkett, S. P., & Socker, D. G. 2009, ApJ, 694, 707
Zhao, X. H., Feng, X. S., Xiang, C. Q., Liu, Y., Li, Z., Zhang, Y., & Wu, S. T. 2010, ApJ, 714, 1133